Research in Computational Fluid Dynamics, Stimulated by ERCIM

Jean-Antoine Désidéri
INRIA Sophia-Antipolis

Pieter W. Hemker
Barry Koren
CWI

Marie-Hélène Lallemand
INRIA Rocquencourt

1 Introduction

During the last six years, by his spoken and written words in support of ERCIM [1] [2] [3] [4], Prof. Baayen has stimulated cooperation between fellow researchers at European sister institutes. Baayen's words were not just pie in the sky. Already in 1988, financial and logistic support became available for mutual working visits of ERCIM researchers. Based on earlier contacts, the authors could soon take advantage of these newly created ERCIM opportunities. Without encountering any red-tape, the authors could start joint ERCIM work in the field of computational fluid dynamics. This led to several papers in the international scientific literature. This contribution gives a survey of some of this research, which is described in more detail in two SIAM articles[5] [6]. It is our tribute to Prof. Baayen's inspiring role as the first ERCIM president.

[1] P.C. Baayen, A. Bensoussan, G. Seegmüller, European computer science market, *CWI GMD INRIA Newsletter*, **1**, p. 1, 1989.

[2] P.C. Baayen, ERCIM's joint action programme is taking shape, *CWI GMD INRIA Newsletter*, **3**, p. 1, 1990.

[3] P.C. Baayen, Strengthening ERCIM, *ERCIM News*, **11**, p. 2, 1992.

[4] P.C. Baayen, Editorial, *ERCIM News*, **15**, p. 1, 1993.

[5] M.-H. Lallemand and B. Koren, Iterative defect correction and multigrid accelerated explicit time stepping schemes for the steady Euler equations, *SIAM Journal on Scientific Computing*, **14**, p. 953-970, 1993.

[6] J.-A. Désidéri and P.W. Hemker, Analysis of the convergence of iterative implicit and defect correction algorithms for hyperbolic problems, *SIAM Journal on Scientific Computing* (to appear, Jan. 1995).

2 Iterative defect correction and multigrid accelerated explicit time stepping for the steady Euler equations

Convergence results are presented for a new pseudo-unsteady solution method for higher-order accurate upwind discretisations of the steady Euler equations. Comparisons are made with an existing pseudo-unsteady solution method. Both methods make use of nonlinear multigrid for acceleration and nested iteration for the fine-grid initialisation. The new method uses iterative defect correction (ItDeC). This section is based on the paper [9].

2.1 Equations

The equations considered are the steady, two-dimensional, compressible Euler equations

$$\frac{\partial F(W)}{\partial x} + \frac{\partial G(W)}{\partial y} = 0, \tag{2.1}$$

where

$$W = \begin{pmatrix} \rho \\ \rho u \\ \rho v \\ \rho e \end{pmatrix}, \tag{2.2a}$$

$$F(W) = \begin{pmatrix} \rho u \\ \rho u^2 + p \\ \rho uv \\ \rho u(e + \frac{p}{\rho}) \end{pmatrix}, \quad G(W) = \begin{pmatrix} \rho v \\ \rho vu \\ \rho v^2 + p \\ \rho v(e + \frac{p}{\rho}) \end{pmatrix}. \tag{2.2b}$$

Assuming a perfect gas, the total energy e satisfies: $e = \frac{1}{\gamma - 1}\frac{p}{\rho} + \frac{1}{2}(u^2 + v^2)$. The ratio of specific heats γ is assumed to be constant.

2.2 Spatial discretisation

The computational grid is obtained by a hybrid finite element - finite volume partition. A (possibly unstructured) finite-element triangularisation is used as the basic partition. A cell-centered finite-volume partition is derived from the finite-element partition by connecting the centers of the triangle sides in the manner illustrated in Figure 1.1. The finite-volume grid gives us the easy possibility of grouping together the nodes associated with contiguous finite volumes. If we take unions of control volumes this results in a new coarser mesh. Repetition of this operation gives coarser and coarser meshes. For details about the coarsening process (multilevel gridding) we refer to [8].

On the finest grid, for all finite volumes C_i, $i = 1, 2, \ldots, N$, we consider the integral form

$$\oint_{\partial C_i} (F(W)n_x + G(W)n_y)\, ds = 0, \quad i = 1, 2, \ldots, N, \tag{2.3}$$

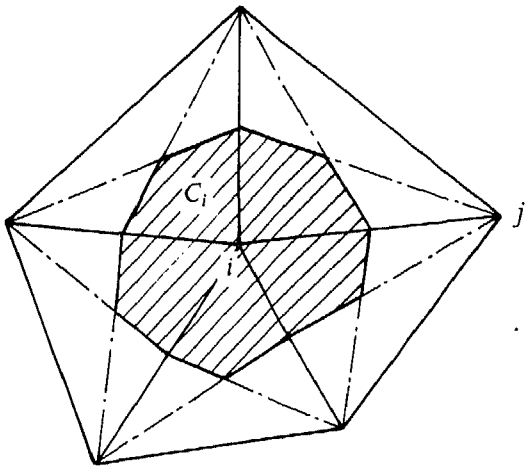

FIGURE 2.1. Finite volume C_i

with n_x and n_y the x- and y-component of the outward unit normal on the volume boundary ∂C_i. For the Euler equations, because of their rotational invariance, (1.3) may be rewritten as

$$\oint_{\partial C_i} T^{-1}(n_x, n_y) F(T(n_x, n_y)W) ds = 0, \quad i = 1, 2, \ldots, N, \tag{2.4}$$

where $T(n_x, n_y)$ is the rotation matrix

$$T(n_x, n_y) = \begin{pmatrix} 1 & 0 & 0 & 0 \\ 0 & n_x & n_y & 0 \\ 0 & -n_y & n_x & 0 \\ 0 & 0 & 0 & 1 \end{pmatrix}. \tag{2.5}$$

For simplicity, we assume the flux to be constant across each bi-segment ∂C_{ij} of the boundary ∂C_i, where $\partial C_{ij} = \partial C_i \cap \partial C_j$ is the common boundary between the neighbouring volumes C_i and C_j (Figure 1.2a). Hence, $\partial C_i = \cup \partial C_{ij}$, $j = 1, 2, \ldots, n_i$, with n_i the number of neighbouring volumes C_j. (In the example of Figure 1.1: $n_i = 5$.) Since we have assumed that the flux is constant along ∂C_{ij}, it is equal to the flux across the straight segment $\bar{\partial} C_{ij}$ connecting the two extreme points of ∂C_{ij} (Figure 1.2b). If we introduce the outward unit normal $\bar{n}_{ij} = ((\bar{n}_x)_{ij}, (\bar{n}_y)_{ij})^T$ along each $\bar{\partial} C_{ij}$, $j = 1, 2, \ldots, n_i$, with the assumption of a constant flux, the contour integral (1.4) can be rewritten as the sum

$$\sum_{j=1}^{n_i} \bar{T}_{ij}^{-1} F(\bar{T}_{ij} W_{ij}) l_{ij} = 0, \quad i = 1, 2, \ldots, N, \tag{2.6}$$

a. Bi-segment ∂C_{ij} b. Straight segment $\bar{\partial} C_{ij}$

FIGURE 2.2. Segments in between finite volumes C_i and C_j

where $\bar{T}_{ij} = T((\bar{n}_x)_{ij}, (\bar{n}_y)_{ij})$, where W_{ij} is some value of W depending on for instance W_i and W_j, and where l_{ij} is the length of the segment $\bar{\partial} C_{ij}$.

Crucial in (1.6) is the way in which the cell-face flux $F(\bar{T}_{ij} W_{ij})$ is evaluated. For this we use an upwind scheme which follows the Godunov principle [3], which assumes that the constant flux vector along each segment $\bar{\partial} C_{ij}$ is determined only by a uniformly constant left and right cell-face state (W_{ij}^l and W_{ij}^r). The 1D Riemann problem which then arises at each cell face is solved in an approximate way. With this, (1.6) can be further rewritten as

$$\sum_{j=1}^{n_i} \bar{T}_{ij}^{-1} \Phi(\bar{T}_{ij} W_{ij}^l, \bar{T}_{ij} W_{ij}^r) l_{ij} = 0, \quad i = 1, 2, \ldots, N, \tag{2.7}$$

where Φ denotes the approximate Riemann solver. Several approximate Riemann solvers exist. In the present paper we apply that of Osher and Solomon [11].

The flux evaluation, and so the space discretisation, may be either first- or higher-order accurate. First-order accuracy is obtained in the standard way; at each finite-volume wall, the left and right cell-face state which have to be inserted in the numerical flux function are taken equal to those in the corresponding adjacent volumes:

$$W_{ij}^l = W_i, \quad W_{ij}^r = W_j. \tag{2.8}$$

Whereas the first-order accurate discretisation is applied at all levels, the higher-order discretisation is applied at the finest grid only, using the finite-element partition existing there. Higher-order accuracy is obtained with a MUSCL-approach [10]. Here, W_{ij}^l and W_{ij}^r are derived from linear interpolations. On each volume C_i around the triangle-vertex i an approximate gradient, denoted by $(\bar{\nabla} W)_i$, is derived by integrating the gradient of the linear inter-

polant of W over all the triangles which have i as a vertex:

$$(\bar{\nabla}W)_i = \left(\left(\frac{\bar{\partial}W}{\partial x} \right)_i, \left(\frac{\bar{\partial}W}{\partial y} \right)_i \right)^T, \quad \text{with} \tag{2.9a}$$

$$\left(\frac{\bar{\partial}W}{\partial x} \right)_i = \frac{\int_{\text{supp}(i)} \frac{\partial W}{\partial x}\, dx\, dy}{\int_{\text{supp}(i)} dx\, dy}, \quad \left(\frac{\bar{\partial}W}{\partial y} \right)_i = \frac{\int_{\text{supp}(i)} \frac{\partial W}{\partial y}\, dx\, dy}{\int_{\text{supp}(i)} dx\, dy}. \tag{2.9b}$$

In here, supp(i) denotes the union of triangles which have i as a vertex. Then for each pair of neighbouring vertices (i, j) we compute the extrapolated values

$$W_{ij}^l = W_i + \frac{1}{2}(\bar{\nabla}W)_i \cdot \bar{ij}, \quad W_{ij}^r = W_j - \frac{1}{2}(\bar{\nabla}W)_j \cdot \bar{ij}. \tag{2.10}$$

On equidistant grids, this higher-order accurate discretisation can be formally proved to be second-order accurate. The proof is still valid for nearly equidistant grids.
In order to ensure monotonicity, while preserving the higher-order accuracy in smooth flow regions, the higher-order values W_{ij}^l and W_{ij}^r according to (1.10) can be replaced by limited values which do not affect the order of accuracy.

2.3 Existing solution method

To solve the steady discretised system (1.7), we consider the unsteady, semi-discrete system of ordinary differential equations

$$\frac{dW_i}{dt} = R_i, \quad i = 1, 2, \ldots, N. \tag{2.11}$$

The natural choice for R_i is

$$R_i = \frac{-1}{A_i} \sum_{j=1}^{n_i} \bar{T}_{ij}^{-1} \Phi(\bar{T}_{ij} W_{ij}^l, \bar{T}_{ij} W_{ij}^r) l_{ij}, \tag{2.12}$$

where A_i is the area of finite volume C_i.

As an upwind analogue to Jameson's central method (Jameson 1983), in [8] an explicit four-stage Runge-Kutta (RK4-) scheme is applied for the temporal integration of (1.11)-(1.12). The benefits of the upwind analogue are evident: better shock capturing, greater robustness and no tuning of explicitly added artificial viscosity. Similarly, just as in [6], in [8] multigrid is applied for accelerating the solution process. Furthermore, just as in [6], time accuracy is not pursued and optimal Runge-Kutta coefficients are applied to get good stability as well as good smoothing properties. It seems that the solution method presented in [8] is already competitive with Jameson's method, without the introduction of a further acceleration technique such as for example residual averaging.

It is of interest that the upwind analogue allows a further efficiency improvement by exploitation of the direct availability of the corresponding first-order

upwind discretisation, with its better stability and smoothing properties. Since a first-order central discretisation is not readily available, a standard central method does not easily allow this improvement.

2.4 *Improved solution method*

Compared with the existing solution method, the new solution method only uses a more extensive right-hand side in the explicit time-stepping scheme. The extension consists of two first-order upwind defects, one which is evaluated at each stage of the multistage scheme, and another which is kept frozen during a fixed number of ν_t RK4-time-steps ($\nu_t \geq 1$) and which compensates for the other first-order defect by its opposite sign. Further - which is important - the higher-order defect is kept frozen as well during ν_t RK4-steps. The four-stage time-stepping scheme is given in Table 1. In here, ν is the time-step number, k the stage number, Δt_i the local time step and α_k the k-th Runge-Kutta coefficient. In the existing higher-order method the right-hand side $R_i^{\nu,k-1}$ is

$$R_i^{\nu,k-1} = \frac{-1}{A_i} \sum_{j=1}^{n_i} \bar{T}_{ij}^{-1} \Phi(\bar{T}_{ij}(W_{ij}^l)^{\nu,k-1}, \bar{T}_{ij}(W_{ij}^r)^{\nu,k-1}) l_{ij}, \tag{2.13}$$

with $(W_{ij}^l)^{\nu,k-1}$ and $(W_{ij}^r)^{\nu,k-1}$ higher-order accurate. So nothing is kept frozen in the existing method's right-hand side. For the improved method we take

$$\begin{aligned} R_i^{\nu,k-1} = \frac{-1}{A_i} \sum_{j=1}^{n_i} \bar{T}_{ij}^{-1} \Big[& \Phi(\bar{T}_{ij} W_i^{\nu,k-1}, \bar{T}_{ij} W_j^{\nu,k-1}) - \\ & \Phi(\bar{T}_{ij} W_i^{0,0}, \bar{T}_{ij} W_j^{0,0}) + \\ & \Phi(\bar{T}_{ij}(W_{ij}^l)^{0,0}, \bar{T}_{ij}(W_{ij}^r)^{0,0}) \Big] l_{ij}, \end{aligned} \tag{2.14}$$

where only $(W_{ij}^l)^{0,0}$ and $(W_{ij}^r)^{0,0}$ are higher-order accurate. The frozen first-order cell-face states ($W_i^{0,0}$ and $W_j^{0,0}$) and the frozen higher-order cell-face states ($(W_{ij}^l)^{0,0}$ and $(W_{ij}^r)^{0,0}$) are updated in an additional outer iteration, a

TABLE 1. Explicit RK4-scheme

$W_i^{0,4} := W_i^{0,0}, \quad i = 1, 2, \ldots, N$
for ν **from** 1 **to** ν_t **do**
  $W_i^{\nu,0} := W_i^{\nu-1,4}, \quad i = 1, 2, \ldots, N$
  for k **from** 1 **to** 4 **do**
    $W_i^{\nu,k} := W_i^{\nu,0} + \Delta t_i \, \alpha_k \, R_i^{\nu,k-1}, \quad i = 1, 2, \ldots, N$
  enddo
enddo

defect correction iteration. For general information on defect correction processes we refer to [1]. For explanation and analysis of the present defect correction iteration we refer to [9]. Here, we directly procced with an illustration of the performance of the present new method.

2.5 Numerical results

In [9], by analysis we found that the new higher-order method has better stability and smoothing properties than the existing higher-order method. In order to verify these predicted better stability and convergence properties, we compute the standard transonic channel flow from [12] with the two-dimensional Euler equations. Three finest grids are considered: a 161-vertices grid, an about twice as fine 585-vertices grid and an about four times as fine 2225-vertices grid. (See [8] for more grid details.) The corresponding solution schedules applied are a 4-, 5- and 6-levels schedule ($L = 4, 5, 6$), respectively, all with $\nu_{\text{pre}} = \nu_{\text{post}} = 1$, $\forall l$. (For the definition of symbols we refer to [9].)

In Figure 1.3a we present various convergence histories as obtained for $L = 4, 5, 6$, respectively. The convergence results presented are:

- those of the first-order discretised Euler equations solved by means of the nonlinear multigrid iteration (dotted lines),
- those of higher-order discretised Euler equations solved by means of the existing higher-order method (dashed lines), and
- those of higher-order discretised Euler equations solved by means of the improved higher-order method (solid lines).

In all three graphs in Figure 1.3a, the residual considered is the L_2-norm of the error in the conservation of mass over all the finest-grid cells. Further, in all three graphs, the number of cycles indicated along the horizontal axis is:

- the number of FAS-cycles in case of both the first-order method and the existing higher-order method, and
- the number of ItDeC-cycles in case of the new higher-order method.

Note that with the new higher-order method, for $\nu_{\text{FAS}} = 2, 5, 10$ the number of inner FAS-cycles is respectively 2, 5 and 10 times larger than the number of indicated ItDeC-cycles. (Only for $\nu_{\text{FAS}} = 1$, the number of FAS-cycles equals the number of ItDeC-cycles.) All convergence histories start at the end of the FMG-stage ([9]). In agreement with the theoretical results presented in [9], for all four values of ν_{FAS} (so also for $\nu_{\text{FAS}} = 1$), the new method does indeed give a better convergence than the existing higher-order method. For decreasing mesh width, the convergence of the new higher-order method becomes even relatively better than that of the first-order method. (For all four values of ν_{FAS} under consideration, the corresponding convergence histories in Figure 1.3a show a better grid-independency than those of the multigrid method applied to the

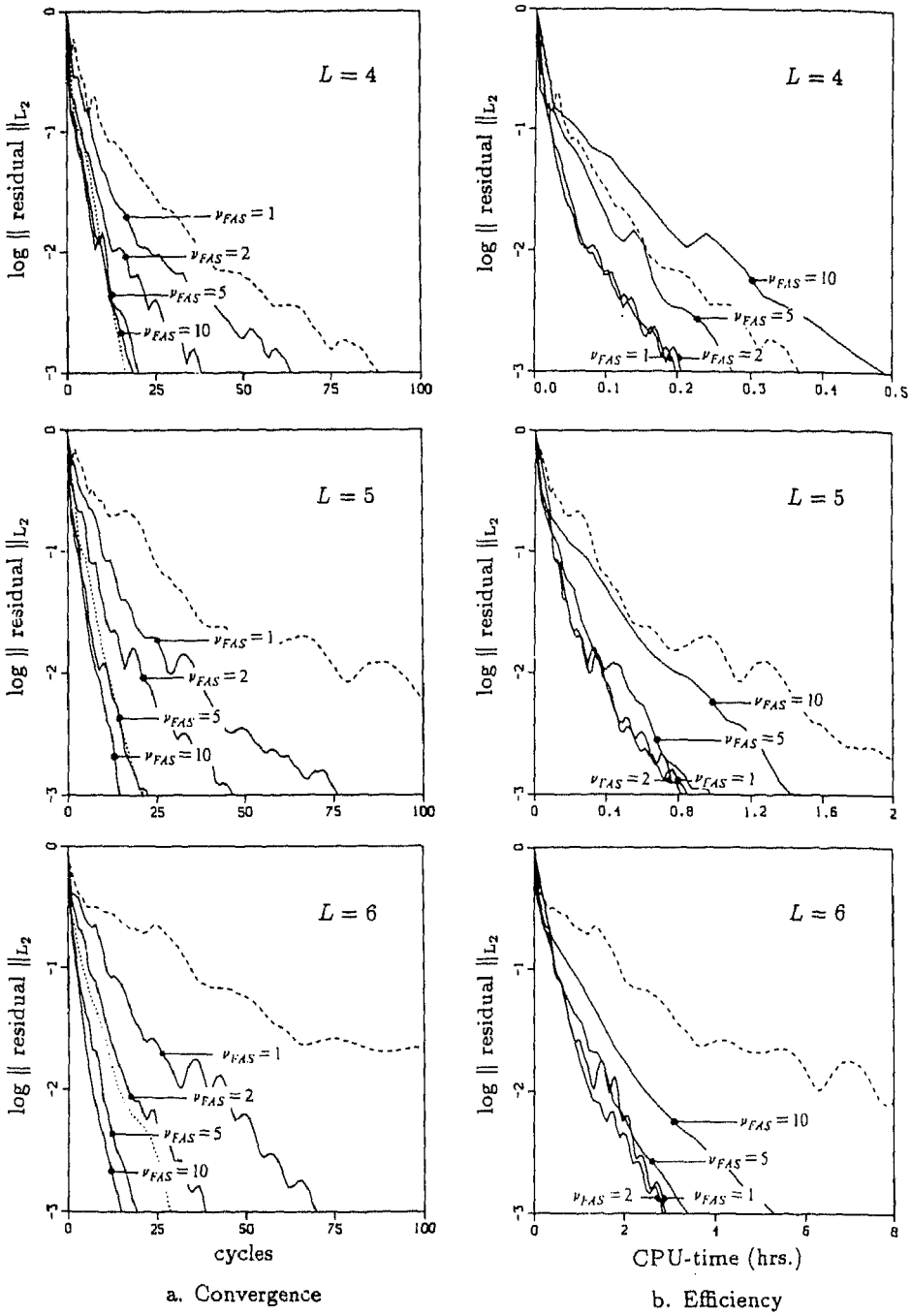

FIGURE 2.3. Convergence and efficiency histories (first-order method: ···, existing higher-order method: – – –, improved higher-order method:)

first-order discretised equations.) This better performance is probably due to the predicted better smoothing in the new method.

As for the actual order of accuracy, if we took the converged higher-order accurate solution obtained on the 2225-vertices grid as the reference solution, we measured local orders of accuracy in the range $[\mathcal{O}(h^{1.4}),\ \mathcal{O}(h^{2.3})]$ for the solutions on the coarser grids (the 585-vertices grid and the 161-vertices grid). The global order of accuracy appears to be almost $\mathcal{O}(h^2)$.

Finally, the important question still remains which of the various higher-order methods is the most efficient. To answer this question, we give the higher-order efficiency histories in Figure 1.3b. (The indicated computing times have been obtained on a Sequent.) Since the sizes of the three grids considered are related to each other by approximately a factor 4, we have related the scales along the horizontal axes accordingly. Concerning the relative efficiency of the improved higher-order method, for the four values of ν_{FAS} considered, it appears that for all three grids the best efficiency is obtained with $\nu_{\mathrm{FAS}} = 1$ (just as in [7], for the schedule with only a single FAS-cycle per ItDeC-cycle.) Further it appears - and this is important - that the improved method with $\nu_{\mathrm{FAS}} = 1$ is also more efficient than the existing higher-order method. Due to the better grid-independency of the improved method, this relatively better efficiency becomes even increasingly better with decreasing mesh width.

2.6 Conclusions

Fully implicit solution methods for higher-order discretised equations may strongly benefit from iterative defect correction when these systems of discretised equations are not easily invertible, which often is the case with higher-order accurate discretisations. Fully explicit solution methods may also profit from iterative defect correction. Here the profits are faster convergence and higher efficiency. The defect correction method appears to lead to greater stability (and hence to greater robustness) than the existing (standard) explicit method. Compared to the existing explicit method it possesses remarkably good smoothing properties, in fact even better than the first-order method. Last but not least its convergence rate appears to be grid-independent. For upwind discretisations, the 'price' which has to be paid for using defect correction iteration - a slightly more complex algorithm - is negligible, because of the direct availability of an appropriate approximate operator: the first-order upwind operator.

3 Convergence behaviour of defect correction for hyperbolic equations

This section is based on the paper [2]. The nonlinear multigrid method is efficient for the solution of the compressible Navier-Stokes equations with a large Reynolds number, or for the Euler equations [5, 7]. The relaxation procedure being the workhorse of the multigrid method, the existence of a relaxation routine suited for fast reduction of the high frequency error components in the

solution of the discrete equations is essential for this success [5]. A good relaxation routine is found in point- or line-wise nonlinear (collective) Gauss-Seidel relaxation, assumed that we solve the first order accurate discrete equations.

For the second order discretisation the relaxation procedures are significantly less efficient. This is the reason why an additional iteration procedure is introduced as an outer loop: iterative defect correction (ItDeC [1]). The second order accurate approximation is now computed by the iteration

$$N_h^1(q_h^{(1)}) = 0, \tag{3.1}$$

$$N_h^1(q_h^{(i+1)}) = N_h^1(q_h^{(i)}) - N_h^2(q_h^{(i)}), \quad i = 1, 2, \cdots. \tag{3.2}$$

Here N_h^1 and N_h^2 denote the first and second order (nonlinear) discrete operators. Only systems for first order accurate discrete equations are solved, but the fixed point of the iteration is the solution of the second order discrete system

$$N_h^2(q_h) = 0. \tag{3.3}$$

For the approximate solution of each iterate $q_h^{(i+1)}$, $i = 0, 1, \cdots$, a small number of multigrid iteration steps (and in many cases only a single step) is sufficient.

It is a classical result that, under easily satisfied conditions, the second iterate $q_h^{(2)}$ is already second order accurate [4, Sect.14.2.2]. This result describes the convergence behaviour for the low-frequency difference between the first and second order discrete approximations. It explains why the convergence is fast for smooth solutions and fine grids. However, for the Navier-Stokes equations with high Reynolds number and for the Euler equations, sharp layers or discontinuities may exist in the solution. Therefore, it is of interest to study the total convergence behaviour for defect correction.

3.1 Linear model problem

In this contribution we restrict ourselves to the Euler equations. These equations form a hyperbolic system of conservation laws. To analyze the convergence for these equations, we first study the linear model problem in two dimensions

$$\frac{\partial}{\partial t}q + a\frac{\partial q}{\partial x} + b\frac{\partial q}{\partial y} = 0. \tag{3.4}$$

Although we are mainly interested in the steady state, we consider here the time-dependent problem in order to introduce a 'flow direction' so that inflow and outflow boundaries can be identified. The vector $(a, b)^T$ determines the flow direction, and with $a > 0$ the flow is in the positive x-direction.

For the first order discretisation, the simple upwind scheme is used. This scheme is described by its stencil

$$L_h^1 \sim \begin{bmatrix} & 0 & \\ -a & a+b & 0 \\ & -b & \end{bmatrix}. \tag{3.5}$$

For the second order discretisation, various alternatives are available. Obvious possibilities are the second order upwind scheme and the central scheme, with the stencils

$$L_h^{2U} \sim \begin{bmatrix} & & 0 & & \\ & & 0 & & \\ \frac{a}{2} & -2a & \frac{3(a+b)}{2} & 0 & 0 \\ & & -2b & & \\ & & \frac{b}{2} & & \end{bmatrix}, \quad \text{and} \quad L_h^{2C} \sim \begin{bmatrix} & -\frac{b}{2} & \\ -\frac{a}{2} & 0 & \frac{a}{2} \\ & -\frac{b}{2} & \end{bmatrix}. \tag{3.6}$$

The corresponding linear operators are denoted by L_h^1, L_h^{2C} and L_h^{2U}, for the first order and the second order central and upwind scheme respectively. By linear combination of L_h^{2C} and L_h^{2U} a scale of second order schemes is obtained, the so-called κ-schemes

$$L_h^{2\kappa} = \frac{1+\kappa}{2} L_h^{2C} + \frac{1-\kappa}{2} L_h^{2U}. \tag{3.7}$$

Here $\kappa \in [-1,1]$ is a free parameter that determines the particular scheme; $\kappa = 0$ corresponds with Fromm's scheme. Being interested in the convergence of ItDeC, we study the amplification operator of the error,

$$M_h^\kappa = (L_h^1)^{-1}(L_h^1 - L_h^{2\kappa}). \tag{3.8}$$

3.2 One-dimensional analysis

We first study the operator M_h^κ in the one-dimensional case. Then, without loss of generality, we have

$$L_h^1 \sim [-1, 1, 0], \quad \text{and} \tag{3.9}$$

$$L_h^{2\kappa} \sim \frac{1+\kappa}{4}[-1,0,1] + \frac{1-\kappa}{4}[1,-4,3,0,0]. \tag{3.10}$$

For an infinite, regular grid with mesh width h, eigenfunctions for these operators are u_ω, $\omega \in [-\pi/h, \pi/h]$, where $u_\omega(jh) = e^{i\omega hj}$. Corresponding eigenvalues of the operator M_h^κ are

$$\widehat{M}_h^\kappa(\omega) = i \sin(\omega h/2)\cos(\omega h/2) + \kappa \sin^2(\omega h/2). \tag{3.11}$$

This shows that the eigenvalues are located in the complex plane on an ellipse with axes $x \in [0, \kappa]$, $y \in [-1/2, 1/2]$. From (3.11) we see that the upper bound for the convergence factor is

$$\sup_{\omega \in [-\pi/h, \pi/h]} |\widehat{M}_h^\kappa(\omega)| = \sup_{t \in [0,1)} \sqrt{\kappa^2 t^2 + t(1-t)}\,.$$

Thus, as upper bounds we find

$$\sup_{\omega \in [-\pi/h, \pi/h]} |\widehat{M}_h^\kappa(\omega)| = \frac{1}{2} \frac{1}{\sqrt{1-\kappa^2}} \quad \text{for} \quad \kappa^2 \leq 1/2, \tag{3.12}$$

and

$$\sup_{\omega\in[-\pi/h,\pi/h]} |\widehat{M}_h^\kappa(\omega)| = |\kappa| \quad \text{for} \quad 1/2 \le \kappa^2 \le 1. \tag{3.13}$$

These expressions describe the convergence if no boundaries are present in the domain. To obtain an impression of the influence of the inflow Dirichlet boundary, we consider grid functions on a uniform partition $\{x_i = ih;\ i = 0, 1, 2, ...\}$ of the half-line $[0, \infty)$ and we restrict ourselves to error components that vanish for large x_i. The operators L_h^1 and $L_h^{2\kappa}$ are again described by (3.9), (3.10), except for the first two equations in the system, that are determined by the boundary discretisation.

The eigenfunctions u_λ of M_h^κ and the corresponding eigenvalues λ satisfy the relation $L_h^{2\kappa}\, u_\lambda = (1-\lambda)\, L_h^1\, u_\lambda$, and from (3.10) it follows that u_λ has the form $u_\lambda(jh) = A_0 + A_1\mu_1^j + A_2\mu_2^j$, where μ_1 and μ_2 are roots of the equation

$$\frac{1+\kappa}{2}\,\mu^2 + (2\lambda - \kappa)\,\mu - \frac{1-\kappa}{2} = 0\ .$$

A straightforward computation [2] shows

$$\lambda = \frac{\kappa \pm i\sqrt{1-\kappa^2}\cos\theta}{2}, \qquad \theta \neq 0 \bmod(\pi). \tag{3.14}$$

This shows that all eigenvalues are located on a line segment in the complex plane at a distance $\kappa/2$ from the imaginary axis and that all eigenvalues satisfy $|\lambda| \le \frac{1}{2}$.

In the case $\kappa = \pm 1$, we still have $\rho = \max|\lambda| = 1/2$, but the eigenvalues coalesce and the eigenvectors are no longer independent. Consequently, in the operator decomposition Jordan blocks J arise. In the one-dimensional case, on a finite interval, the size of these blocks is $N-1$, where N is the number of mesh points. Then the convergence behaviour after n iterations of ItDeC is described by $\tau_n = \|J^n\|_\infty$, where

$$J^n = \begin{pmatrix} \rho^n & & & \\ \xi_j^n & \rho^n & & \\ \vdots & \ddots & \ddots & \\ & & \xi_j^n & \rho^n \end{pmatrix}, \quad \text{with} \quad \xi_j^n = \begin{pmatrix} n \\ j \end{pmatrix} \rho^{n-j}\,.$$

It follows that $\tau_n \ge \max_{j=0,1,2,\ldots,N} |\xi_j^n|$, and hence

- it is possible that $\tau \ge 1$ if $n < N$;
- $\tau_n \approx n^{N-1}\rho^n$ for $n \to \infty$, and hence the asymptotic convergence rate of the iteration is $\rho \log|n|$;
- the sequence $\{\tau_\nu\}_{\nu\le n}$ is guaranteed to be decreasing only for $n > N/(1-\rho)$. In our case $\rho = 0.5$. This implies that the iteration may show no convergence for the first $2N$ iteration steps.

These phenomena are seen in practice indeed, as is shown in Figure 3.2.a-d.

If $\kappa \neq \pm 1$ but $1 \leq |\kappa| \leq \frac{1}{2}\sqrt{2}$, the convergence during the first $2N$ iteration steps is dominated by the behaviour as described by the Fourier analysis (3.13), i.e. a convergence rate of $|\kappa|$ is seen. For all $\kappa \in [-1, +1]$ the convergence rate has the lower bound $\rho = 1/2$.

In summary, for the one-dimensional problem we distinguish different phases in the convergence of the iterated defect correction. In most cases we first observe an impulsive start, where all components corresponding with small eigenvalues are damped. For the regular schemes (i.e. $|\kappa|$ different from 1) soon an asymptotic rate of 1/2 is obtained. For the (near) pathological cases (i.e. $|\kappa|$ close to 1), after the impulsive start, we distinguish first a Fourier (or pseudo-convection) phase for about $2N$ iterations, in which the convergence is described by the Fourier analysis. After 2N iterations the asymptotic rate 1/2 is found. In the truly degenerate cases ($|\kappa| = 1$) we recognise a Fourier (pseudo-convection) phase, where the error does not decrease for 2N iterations, and a logarithmic asymptotic rate due to the large Jordan block in the eigenvalue decomposition.

3.3 Two-dimensional analysis

In principle, the Fourier analysis for the two-dimensional difference operators (3.5,3.6) is completely analogous to the one-dimensional case. With the Fourier modes defined by $u_\omega(hj) = e^{i(\omega_1 h_1 j_1 + \omega_2 h_2 j_2)}$, where the subscripts refer to the x- and the y-directions respectively, we find

$$\widehat{L}_h^1(\omega) = 2ia\, e^{-i\omega_1 h_1/2} \sin(\omega_1 h_1/2) + 2ib\, e^{-i\omega_2 h_2/2} \sin(\omega_2 h_2/2)\,, \qquad (3.15)$$

and

$$\begin{aligned} \widehat{L}_h^{2\kappa}(\omega) = \quad & 2ia\, e^{-i\omega_1 h_1/2}\, S_1(C_1^2 + iS_1C_1 + (1-\kappa)S_1^2) + \\ & 2ib\, e^{-i\omega_2 h_2/2}\, S_2(C_2^2 + iS_2C_2 + (1-\kappa)S_2^2)\,, \end{aligned} \qquad (3.16)$$

where $S_1 = \sin(\omega_1 h_1/2)$, $S_2 = \sin(\omega_2 h_2/2)$, $C_1 = \cos(\omega_1 h_1/2)$ and $C_2 = \cos(\omega_2 h_2/2)$.

As the amplification factor we find

$$\begin{aligned} g(\omega) \quad &= \left\| \widehat{M}_h^\kappa(\omega) \right\| = \left\| (\widehat{L}_h^1)^{-1} (\widehat{L}_h^1 - \widehat{L}_h^{2\kappa}) \right\| \\ &= \sqrt{\frac{(a_1 S_1^2(1-(1-\kappa)S_1^2) + a_2 S_2^2(1-(1-\kappa)S_2^2))^2 + (1-\kappa)^2(a_1 S_1^3 C_1 + a_2 S_2^3 C_2)^2}{(a_1 S_1^2 + a_2 S_2^2)^2 + (a_1 S_1 C_1 + a_2 S_2 C_2)^2}}. \end{aligned} \qquad (3.17)$$

This expression can be used to determine the convergence rate for the separate modes on an infinite domain. It shows that, for a given κ, we can never expect a better convergence rate in the two-dimensional case than in the one-dimensional case.

For the analysis of the two-dimensional case on a finite domain, we refer to [2]. Essentially, the results for two space dimensions can be seen as a perturbation

of the results for one dimension. Analogous to the one-dimensional domain, the location of the eigenvalues is shown in Figure 3.1. We now find the eigenvalues not on a line segment in the complex plane, but in a cloud near that line segment. The real part of the eigenvalues is generally larger than is the case in one dimension (for the same κ). This means that the cloud is shifted to the right of the corresponding line segment. For the case of large κ ($\kappa \approx +1$), the cloud is larger than for small κ ($\kappa \approx -1$).

For different values of κ and for different values of N the location of the eigenvalues in the complex plane is shown in Figure 3.1. In this figure the ratio a/b is 2/3.

In Figure 3.2 the convergence behaviour is shown for the model problem on a 40 × 40-mesh. For $\kappa \leq 0$ the cloud of eigenvalues is still contained in the circle $|z| \leq 0.5$, so $\rho(M_h^\kappa) \leq 0.5$ if $\kappa \leq 0$. However, for $0 < \kappa \leq 1$ we find possibly $\rho(M_h^\kappa) > 0.5$, and for large κ we have $\lim_{\kappa \to +1} \lim_{h \to 0} \rho(M_h^\kappa) = 1$. This explains why a convergence rate $\rho(M_h^\kappa) > 0.5$ is found for $\kappa = 1/3$ in Figure 3.2.e whereas $\rho(M_h^\kappa) = 0.5$ for $\kappa = 0$ (Figure 3.2.c). For more details we refer to [2].

3.4 Euler equations

A similar behaviour, depending on κ, as for the linear model problem, is found for the nonlinear Euler equations. In Figure 3.3 we show the convergence behaviour for a problem that describes subsonic flow around a standard NACA0012 airfoil. This is a smooth flow where the problem is described by a complex nonlinear system of equations and the domain is not simply connected. The mesh is 20×32 and results are shown for different values of κ. We see that the iteration doesn't converge for $\kappa = 1$, as it doesn't for $\kappa = -1$ (not shown). We obtain slow convergence for $\kappa = 0.8$ and $\kappa = -0.8$. Good convergence with a rate of approximately 0.5 per iteration step is obtained for $\kappa = 1/3, 0$ and $-1/3$. Probably the asymptotic rate cannot be observed because rounding error accuracy is obtained after approximately 40 iterations. For $\kappa = 1/3$ and $\kappa = -1/3$ we see that after an initial phase with $\rho \approx 0.5$, we obtain another phase with a slightly slower convergence rate. Such effect is not (yet) seen for $\kappa = 0$.

The first order discrete equations are solved by a nonlinear multigrid method [5]. It employs a nonlinear symmetric point-Gauss-Seidel relaxation as a smoother and a nested sequence of Galerkin discretisations for the coarse grid corrections. Experience has shown that a small number of iteration cycles of this multigrid method solves the discrete system to a high degree of accuracy. In the experiments shown, 3 FAS V-cycles were applied for each single defect correction step. It was shown by experiments that the same results were obtained for multigrid iteration with 2 through 5 FAS V-cycles. All initial estimates were obtained by interpolation from a first order accurate solution on a coarser grid.

For this flow subsonic flow around the airfoil $\kappa = 1$ gives an almost diverging

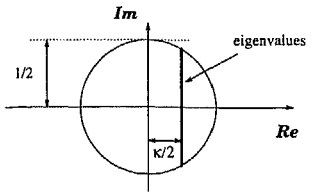

One-dimensional

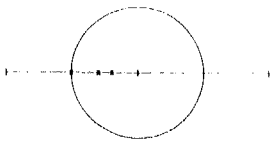

Two-dimensional , $\kappa = -1$

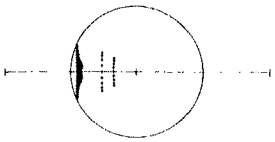

Two-dimensional , $\kappa = -0.9$

Two-dimensional , $\kappa = -2/3$

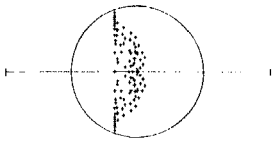

Two-dimensional , $\kappa = -1/3$

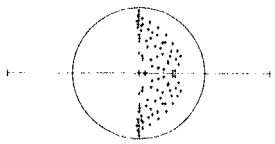

Two-dimensional , $\kappa = 0$

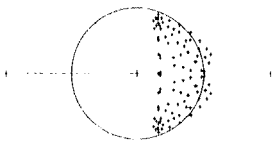

Two-dimensional , $\kappa = 1/3$

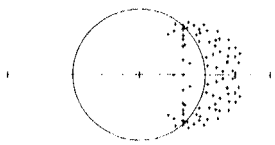

Two-dimensional , $\kappa = 2/3$

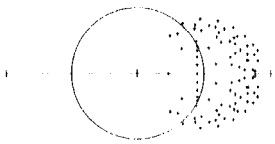

Two-dimensional , $\kappa = 0.9$

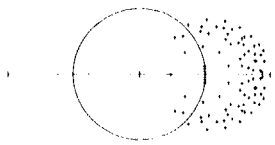

Two-dimensional , $\kappa = 0.99$

FIGURE 3.1. Location of the eigenvalues of the amplification matrix M_h^κ in the complex plane, relatively to the circle of radius 1/2, for the one and the two-dimensional model problem. Except for the first 1-dim. figure, the mesh is 10×10 and the ratio $a/b = 2/3$.

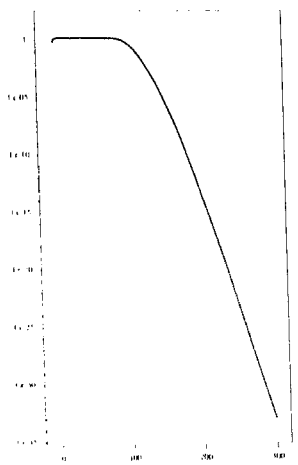

Figure 2.a, 1-dim
$N = 50$; $\kappa = 1$

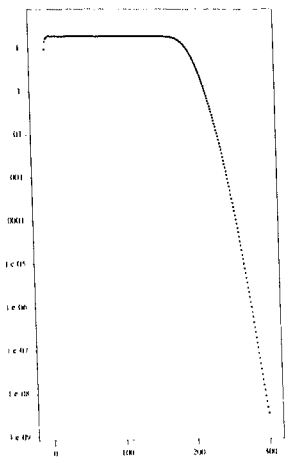

Figure 2.b, 1-dim
$N = 100$; $\kappa = 1$

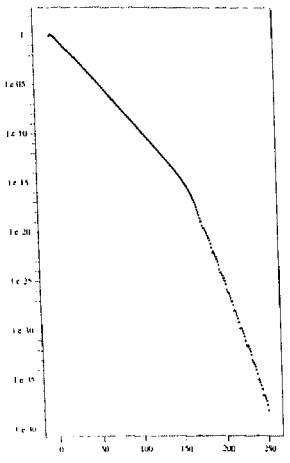

Figure 2.c, 1-dim
$N = 100$; $\kappa = 0.8$

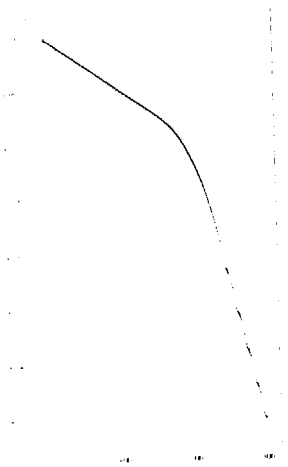

Figure 2.d, 1-dim
$N = 100$; $\kappa = 0.9$

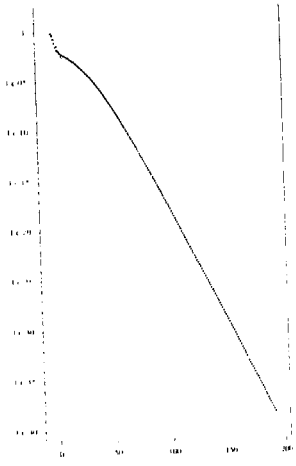

Figure 2.e, 2-dim
40×40 mesh; $\kappa = 1/3$

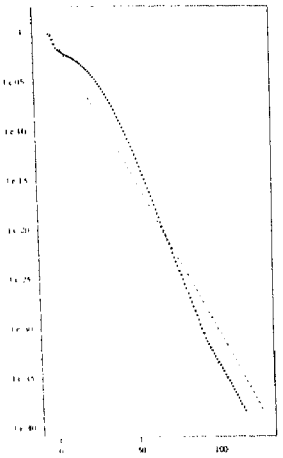

Figure 2.f, 2-dim
40×40 mesh; $\kappa = 0$

The sup-norm of the error is plotted against the number of iterations.
The dashed line corresponds with a convergence rate $\rho = 1/2$.

FIGURE 3.2. Convergence of ItDeC for the one- or two-dimensional linear test problem.

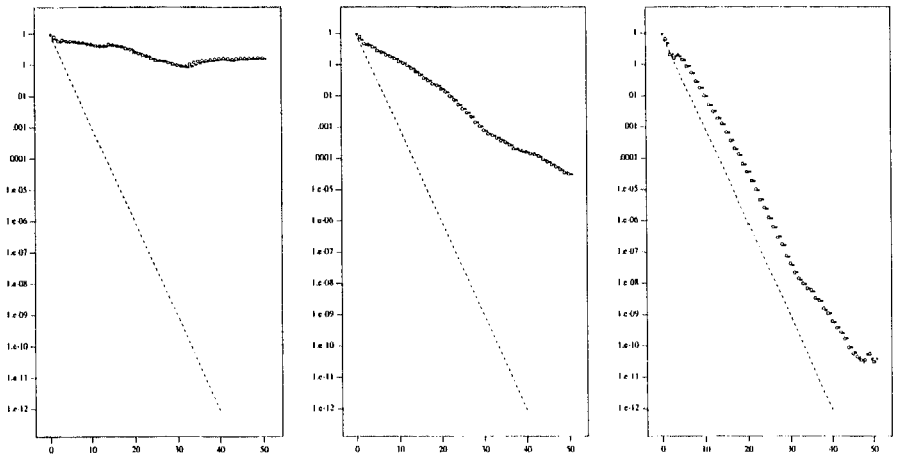

$\kappa = +1$ $\kappa = 0.8$ $\kappa = 1/3$

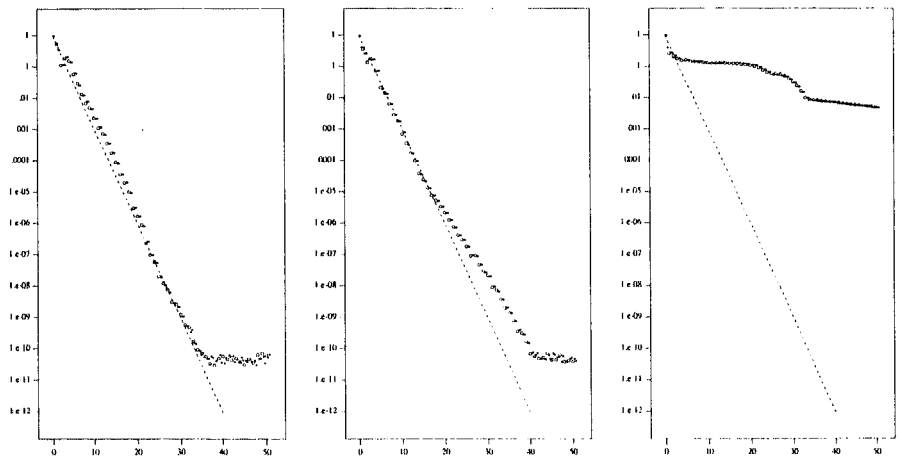

$\kappa = 0$ $\kappa = -1/3$ $\kappa = -0.8$

FIGURE 3.3. Subsonic Flow over a NACA0012 Airfoil
Convergence of the defect-correction method, on a 20×32 mesh.
Mach number at infinity, $M_\infty = 0.63$, and the angle of attack $\alpha = 2.0^o$.
The dashed line corresponds to a convergence rate 1/2.

process and $\kappa = 0.8$ and $\kappa = -0.8$ shows bad convergence. The asymmetry in the convergence behaviour with respect to $\kappa > 0$ (worse) and $\kappa < 0$ (better convergence) might be understood by the location of the eigenvalues in the complex plane (as shown in Figure 3.1). There we see that more eigenvalues are located in the neighbourhood of the origin for $\kappa < 0$ than for $\kappa > 0$. This may be of greater importance for the nonlinear equations, where the corresponding eigenvectors are excited again and again, than for the linear problems, where the effect of these eigenvalues is no longer seen after a sufficient number of iterations.

References

1. K. Böhmer, P.W. Hemker and H.J. Stetter, The defect correction approach, *Computing Suppl.*, **5**, 1-32, 1984.
2. J.-A. Désidéri and P.W. Hemker, Analysis of the convergence of iterative implicit and defect correction algorithms for hyperbolic problems, *SIAM J. Sci. Comput.*, (to appear, Jan. 1995).
3. S.K. Godunov, Finite difference method for numerical computation of discontinuous solutions of the equations of fluid dynamics (Cornell Aeronautical Lab. Transl. from Russian), *Mat. Sbornik*, **47**, 271-306, 1959.
4. W. Hackbusch, *Multi-Grid Methods and Applications*, Springer, Berlin, 1985.
5. P.W. Hemker and S.P. Spekreijse, Multiple grid and Osher's scheme for the efficient solution of the steady Euler equations, *Appl. Numer. Math.*, **2**, 475-493, 1986.
6. A. Jameson, Solution of the Euler equations for two dimensional transonic flow by a multigrid method, *Appl. Math. Comput.*, **13**, 327-355, 1983.
7. B. Koren, Defect correction and multigrid for an efficient and accurate computation of airfoil flows, *J. Comput. Phys.*, **77**, 183-206, 1988.
8. M.-H. Lallemand and A. Dervieux, A multigrid finite element method for solving the two-dimensional Euler equations, *Lecture Notes in Pure and Applied Mathematics*, **110**, 337-363 (S.F. McCormick, ed.), Marcel Dekker, New York, 1988.
9. M.-H. Lallemand and B. Koren, Iterative defect correction and multigrid accelerated explicit time stepping schemes for the steady Euler equations, *SIAM J. Sci. Comput.*, **14**, 953-970, 1993.
10. B. van Leer, Towards the ultimate conservative difference scheme V. A second-order sequel to Godunov's method, *J. Comput. Phys.*, **32**, 101-136, 1979.
11. S. Osher and F. Solomon, Upwind-difference schemes for hyperbolic systems of conservation laws, *Math. Comput.*, **38**, 339-374, 1982.
12. A. Rizzi and H. Viviand (eds.), Numerical Methods for the Computation of Inviscid Transonic Flows with Shock Waves, *Notes on Numerical Fluid Mechanics*, **3**. Vieweg, Braunschweig, 1981.